AIMS Materials Science, 12(4): 909–927.
DOI: 10.3934/matersci.2025040
Received: 03 July 2025
Revised: 28 August 2025
Accepted: 02 September 2025
Published: 10 September 2025

https://www.aimspress.com/journal/Materials

Research article

Influence of Cr substitution on electrical and dielectric properties of monovalent doped Pr-based manganites

Siti Sumaiyah Sheikh Abdul Aziz[1], Nor Asmira Amaran[2], Rozilah Rajmi[3], Sikiru Surajudeen Olalekan[2], Zakiah Mohamed[2] and Norazila Ibrahim[2,*]

[1] Faculty of Applied Sciences, Universiti Teknologi MARA (UiTM), Perak Branch, Tapah Campus, 35400 Tapah Road, Perak, Malaysia
[2] Faculty of Applied Sciences, Universiti Teknologi MARA (UiTM), 40450 Shah Alam, Selangor, Malaysia
[3] Faculty of Applied Sciences, Universiti Teknologi MARA (UiTM), Perlis Branch, Arau Campus, 02600 Arau, Perlis, Malaysia

* **Correspondence:** Email: noraz954@uitm.edu.my; Tel: +603-5544-4478.

Abstract: Polycrystalline $Pr_{0.75}Na_{0.05}K_{0.20}Mn_{1-x}Cr_xO_3$ (x = 0.00, 0.01, 0.02, 0.03, 0.04, 0.05) manganites were synthesized by the solid-state reaction method to examine the role of Chromium (Cr) substitution on structural, electrical, and dielectric behavior. X-ray diffraction (XRD) with Rietveld refinement confirmed a single-phase orthorhombic (Pnma) structure with Cr^{3+} incorporation at Mn^{3+}/Mn^{4+} sites, reflected in compositional changes of unit cell volume. Field-emission scanning electron microscopy (FESEM) revealed grain refinement with increasing Cr, indicating inhibited grain growth and enhanced grain boundary density. Impedance spectroscopy showed a conduction shift from bulk-dominated ($x \leq 0.02$) to grain boundary-controlled ($x \geq 0.03$), with higher Cr levels producing non-Debye relaxation due to carrier localization. Dielectric studies demonstrated frequency-dependent dispersion, where Cr substitution suppressed dielectric constant, dielectric loss, and loss tangent by reducing space-charge and grain boundary effects. The x = 0.02 composition exhibited the most stable dielectric response. These findings establish Cr doping as an effective strategy for tailoring structure-property correlations and enhancing dielectric stability in perovskite manganites.

Keywords: microstructure; dielectric properties; grain boundaries; grain size; perovskites

1. Introduction

The investigation of manganites, especially those infused with rare earth elements, has attracted considerable interest in the realm of condensed matter physics because of their distinctive magnetic, electrical, and dielectric characteristics [1,2]. The study of manganites with the general formula, $A_{1-x}B_xMnO_3$, (where A stands for trivalent rare-earth ions like Pr^{3+}, Nd^{3+}, Ca^{2+}, Sr^{2+}, and La^{3+} [3] and B stands for divalent (Ca^{2+}, Ag^{2+}) or monovalent alkaline earth (Na^+, Li^+, K^+) [4,5]) has attracted considerable interest due to their fascinating electrical and magnetic characteristics, which hold great potential for technological uses [6–8]. Praseodymium (Pr)-based manganites are particularly intriguing due to their intricate interaction between charge, spin, and orbital degrees of freedom [9,10]. These interactions, in combination with variables such as doping, magnetic fields, and temperature, give rise to complex phase diagrams and remarkable phenomena such as colossal magnetoresistance (CMR) [11]. A notable feature of Pr-based manganites is their tunability through substitutional doping, whereby the introduction of foreign ions can drastically alter their structural, electronic, and magnetic responses [12]. Doping at the Mn-site is especially effective because it directly modifies the Mn^{3+}/Mn^{4+} ratio, alters double-exchange interactions, and influences polaron dynamics [11,13]. Among possible dopants, chromium (Cr^{3+}) is of particular interest, with its electronic configuration ($3d^3$, t^3_{2g} e^0_g) [14], is like Mn^{3+} ion ($3d^3$, t^3_{2g} e^1_g) but lacks the itinerant electron (e_g), thereby suppressing Jahn-Teller distortions and modifying the Mn-O-Mn superexchange pathways [14]. Cr-substitution can disrupt long-range double-exchange conduction, enhance electron–phonon coupling, and promote small-polaron formation [15,16]. Reports have shown that Cr incorporation in manganites reduces electrical conductivity and can enhance dielectric performance via grain boundary effects [17], but the detailed relationship between Cr-induced microstructural evolution and dielectric response, particularly in Na/K co-doped Pr-based systems, remains largely unexplored.

Furthermore, while many researchers have addressed Cr doping in La- or Nd-based manganites [14], $Pr_{0.75}Na_{0.05}K_{0.20}MnO_3$ represents a unique compositional space where dual alkali-metal doping (Na^+ and K^+) at the A-site may introduce additional lattice strain and chemical disorder, potentially amplifying the influence of B-site by Cr substitution. This combination has not been systematically investigated for its impedance and dielectric behavior. Thus, in this work, we focus on the effect of Cr substitution at the B-site in $Pr_{0.75}Na_{0.05}K_{0.20}MnO_3$ by linking Cr-induced grain size evolution to electrical transport and dielectric relaxation mechanisms.

Recent advances in synthesis techniques, particularly the sol-gel method, have demonstrated that precise control over particle size and morphology can significantly influence the dielectric performance of perovskite manganites [18]. Sol-gel processing often yields finer, and more uniform grains compared to conventional solid-state methods, increasing grain boundary density and altering polarization mechanisms [18]. Although microstructural tailoring via sol-gel synthesis has been reported for other rare-earth manganites, systematic studies combining Cr substitution, dual alkali doping, and microstructure-dielectric correlations are scarce. In particular, how Cr-induced grain refinement and boundary modifications influence grain and grain boundary contributions in Pr-based manganites remains an open question.

In this study, Cr-doped $Pr_{0.75}Na_{0.05}K_{0.20}MnO_3$ (x = 0.00, 0.01, 0.02, 0.03, 0.04, 0.05) samples are prepared using the solid-state synthesis method and characterized using impedance spectroscopy over a broad frequency range (100 Hz to 1 MHz) at room temperature. Our focus of this research is on the Pr-based manganites system where Cr doping at the Mn site is expected to induce significant changes

in the electrical and dielectric properties of the materials. Our findings contribute to a deeper understanding of the dielectric and electrical properties of Cr-doped manganites, offering potential pathways for optimizing these materials for specific applications. By systematically varying the Cr concentration and employing impedance spectroscopy, the research provides novel insights into the role of Cr doping in influencing grain boundary and grain resistance, as well as the dielectric behavior of the material. Equivalent circuit modeling was employed to distinguish grain and grain boundary resistances, while dielectric constant, dielectric loss, and tangent loss were analyzed as functions of frequency and Cr content. The results provide new insights into the microstructure-driven tuning of dielectric and electrical behavior in complex perovskites, revealing the pivotal role of Cr in regulating conduction pathways and relaxation processes. By addressing the compositional and microstructural dimensions, this study advances the understanding of Pr-based manganites for applications in high-performance electronic devices [19–21], magnetic sensors [19], non-volatile memory elements [20], and energy storage systems [22].

2. Materials and methods

2.1. Preparation of samples

$Pr_{0.75}Na_{0.05}K_{0.20}Mn_{1-x}Cr_xO_3$ (x = 0.00, 0.01, 0.02, 0.03, 0.04, 0.05) manganites were synthesized using solid-state method. High-purity precursors of Pr_6O_{11}, Na_2CO_3, K_2CO_3, MnO_2, and Cr_2O_3 were accurately weighed and mixed in an agate mortar according to their stoichiometric ratios. The resultant powder was thoroughly ground then subjected to calcination twice in a Carbolite furnace (model CWF 11/5) at 950 °C for 24 h with a heating rate of 15 °C/min and a cooling rate of 5 °C/min, including intermediate grinding steps. Following calcination, the powders were reground and pressed into pellets at high pressure (5 tons) using a hydraulic pellet press (model Specac). The pellets had a diameter of 13 mm and a thickness of 3 mm. The samples were then sintered in air at 1100 °C for 36 h, with a slow cooling at a rate of 1 °C /min to achieve oxygen stoichiometry.

2.2. Characterization of samples

Electrical measurements were performed by applying an AC voltage of 1.8 V across the samples using an LCR meter (model HIOKI 3532-50 LCR HiTESTER), interfaced with a computer. The pellet samples were positioned between two stainless steel electrodes with a diameter of 1.5 cm. Measurements were conducted at room temperature over a frequency range of 100 Hz to 1 MHz. A micrometer screw gauge was used to determine the electrode area and the thickness of the samples. From the LCR meter data, a graph of impedance, real (Z') and imaginary parts ($-Z''$ versus Z') was plotted and analyzed using *Z-view Software 2.0.*

3. Results and discussion

3.1. Structural analysis

X-ray diffraction (XRD) analysis confirms that $Pr_{0.75}Na_{0.05}K_{0.20}Mn_{1-x}Cr_xO_3$ (x = 0–0.05) crystallizes in a single-phase orthorhombic *Pnma* structure without detectable impurities. Rietveld refinement

results provide clear evidence of successful Cr^{3+} incorporation into the manganite lattice. Moreover, changes in unit cell volume with composition indicate that Cr^{3+} can substitute at both Mn^{3+} and Mn^{4+} sites, with the initial expansion at x = 0.01 attributed to partial replacement of the smaller Mn^{4+}, followed by contraction at higher doping levels due to dominant substitution of Mn^{3+}. This behavior, consistent with trends reported for other Cr-doped perovskites, highlights the role of ionic size mismatch in influencing lattice parameters and MnO_6 octahedral stability. The detailed structural parameters and full phase analysis have been comprehensively discussed in our previous publication [23]. Furthermore, X-ray photoelectron spectroscopy (XPS) analysis confirms the coexistence of mixed Mn^{3+}/Mn^{4+} states and the successful substitution of Cr^{3+} in $Pr_{0.75}Na_{0.05}K_{0.20}Mn_{1-x}Cr_xO_3$, consistent with reported values for related manganite systems, with the complete dataset published in our earlier work [23].

3.2. Morphological analysis

The field-emission scanning electron microscopy (FESEM) images (Figure 1) of $Pr_{0.75}Na_{0.05}K_{0.20}Mn_{1-x}Cr_xO_3$ (x = 0–0.05) show the evolution of grain morphology with Cr substitution. The inset in each image presents the corresponding grain size distribution histogram with fitted Gaussian curves, from which the average grain sizes are estimated to be 1.90, 2.30, 2.40, 6.60, 3.10, and 3.90 μm, respectively. For x = 0, the grains are irregular in shape, exhibit a broad size distribution (average ≈1.9 μm), and display visible porosity, suggesting incomplete grain growth during sintering. This morphology indicates non-uniform densification, with loosely packed grains separated by pores that can act as scattering centers for charge carriers. When a small amount of Cr is added (x = 0.01–0.02), the grains become more rounded and closely packed, with average sizes of ≈2.3–2.4 μm, likely due to the slight lattice distortion introduced by low Cr doping.

When the Cr content exceeds x = 0.03, the average grain size gradually decreases, and the grain boundaries become more prominent, where the average grain size increases sharply to ≈6.6 μm. Larger grains result in fewer grain boundary barriers, which can facilitate conduction across the grains. When the Cr content increases further (x = 0.04–0.05), the average grain size decreases to ≈3.10 μm for x = 0.04 and ≈3.90 μm for x = 0.05. In these samples, the grains appear less uniform, with more distinct grain boundaries and increased porosity. This suggests that higher Cr levels slow grain growth, likely by hindering grain boundary movement or changing the way atoms diffuse during sintering. These microstructural changes affect electrical behavior. Larger grains at low Cr levels have fewer grain boundaries, so electrical conduction is mainly through the grains, with lower resistance. In contrast, smaller grains at higher Cr levels have more grain boundaries, which can block charge carriers and increase resistivity at low temperatures. Overall, Cr doping appears to control the balance between conduction through grains and across grain boundaries, a point that will be discussed in the following section.

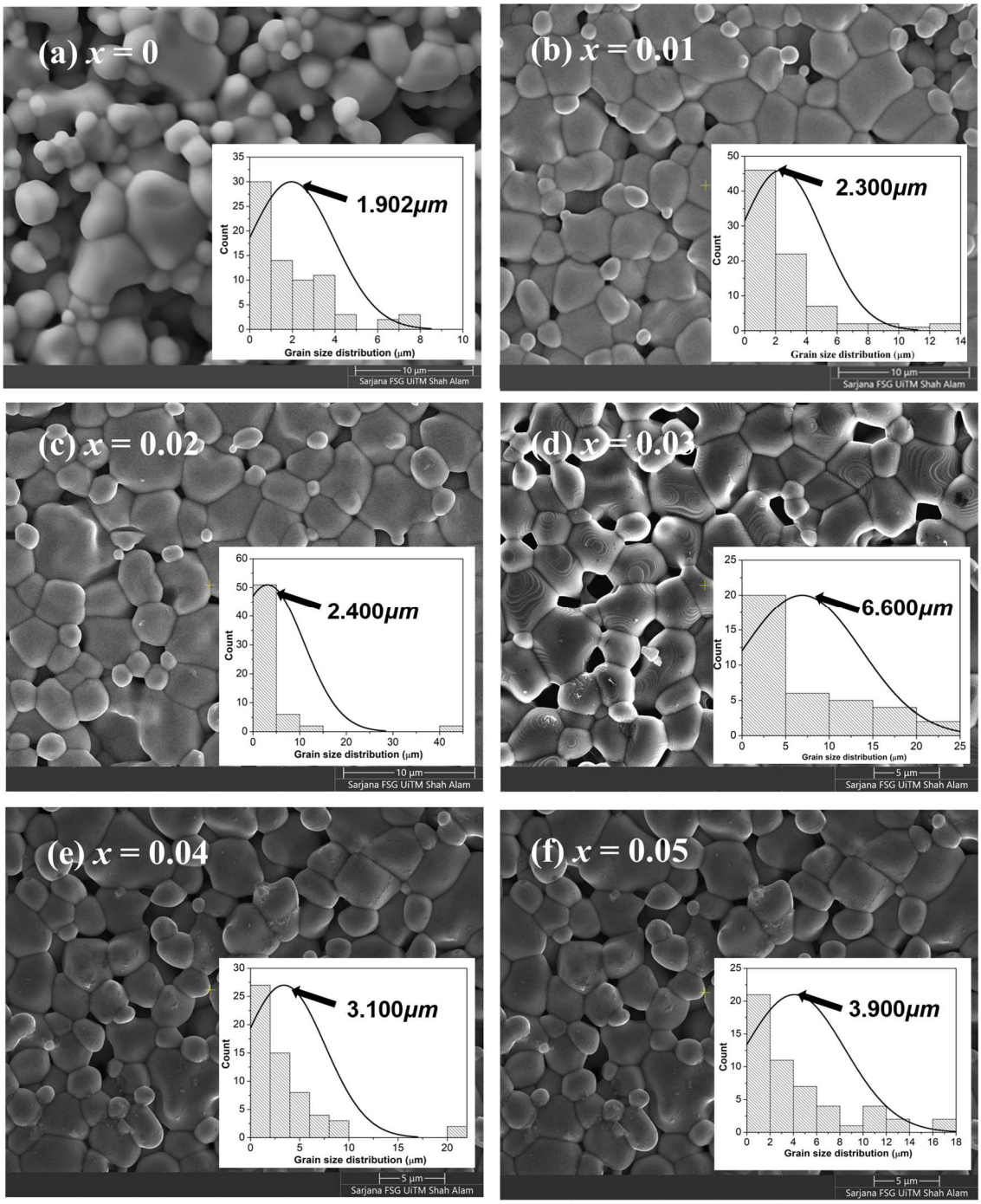

Figure 1. FESEM micrograph for $Pr_{0.75}Na_{0.05}K_{0.20}Mn_{1-x}Cr_xO_3$: (a) 0, (b) 0.01, (c) 0.02, (d) 0.03, (e) 0.04, and (f) 0.05 compounds with 10k magnification. The inset show the corresponding grain size distribution histograms with average grain size values.

3.3. Impedance analysis

The electrical transport behavior, investigated through impedance spectroscopy, further supports microstructural observations in previous section. Figure 2 shows the complex impedance plots, Z'' against Z' of $Pr_{0.75}Na_{0.05}K_{0.20}Mn_{1-x}Cr_xO_3$ manganite for x = 0–0.05 samples with frequencies ranging

from 100 Hz to 1 MHz at room temperature (303 K). The complex impedance data can be represented by its real (Z') and imaginary parts (Z'') using the relation as given in Eq 1 [22,24,25]:

$$Z(\omega) = Z'(\omega) + jZ''(\omega) \quad (1)$$

where ω is angular frequency ($\omega=2\pi f$), and f is frequency of the material. The impedance plots for $x = 0$ show typical impedance behavior, which consists of depressed semicircles at low and high frequencies, with their centers depressed below the real axis. The low-frequency semicircle represents the conduction process from a grain boundary, while the higher-frequency semicircle corresponds to the grain (bulk). This behavior indicates that the relaxation process is not of the Debye type. There is favorable agreement when comparing results from this work against published data [11]. Cr substitution at $x = 0.01$ results in a similar depressed semicircle with an increase in diameter of impedance, indicating higher resistance, possibly due to enhanced grain boundary scattering from the slightly refined grains.

Further substitution of Cr at $x = 0.02$ reveals an inclined spike at high frequency of the spectrum, signifying that conduction is increasingly dominated by intragrain transport. This straight-line behavior indicates that the sample has more conductive grains than grain boundaries. At $x = 0.03$, a significant change in the shape of the semicircular arcs is observed, with two semicircles present, indicating the presence of two relaxation processes (Figure 2d). This behavior reflects coexisting grain and grain boundary relaxation processes. Data dispersion in certain frequency regions may be attributed to electrode-sample interface effects [26], as shown in the inset of Figure 2c,d.

High substitution of Cr at $x = 0.04$ and $x = 0.05$ results in larger Nyquist arcs and more depressed semicircle, with high-frequency intercepts that suggest significant grain contributions and reduced grain boundary conductivity. The increasing arc diameter and shift toward higher Z' values with Cr content corresponds to reduced overall conductivity, consistent with smaller grain sizes and enhanced carrier scattering at grain boundaries [23].

Cr doping progressively refines the grain structure, increasing the density of grain boundaries and altering the balance between grain and grain boundary conduction. The variation in Nyquist arc morphology in diameter, curvature, and frequency response mirrors these microstructural changes, highlighting how Cr substitution tunes the charge transport pathways by modifying both the physical microstructure and the electronic properties. These findings reinforce the strong coupling between doping-induced structural evolution and dielectric/electrical transport behavior in this manganite system; a relationship further explored through equivalent circuit modeling in the next section.

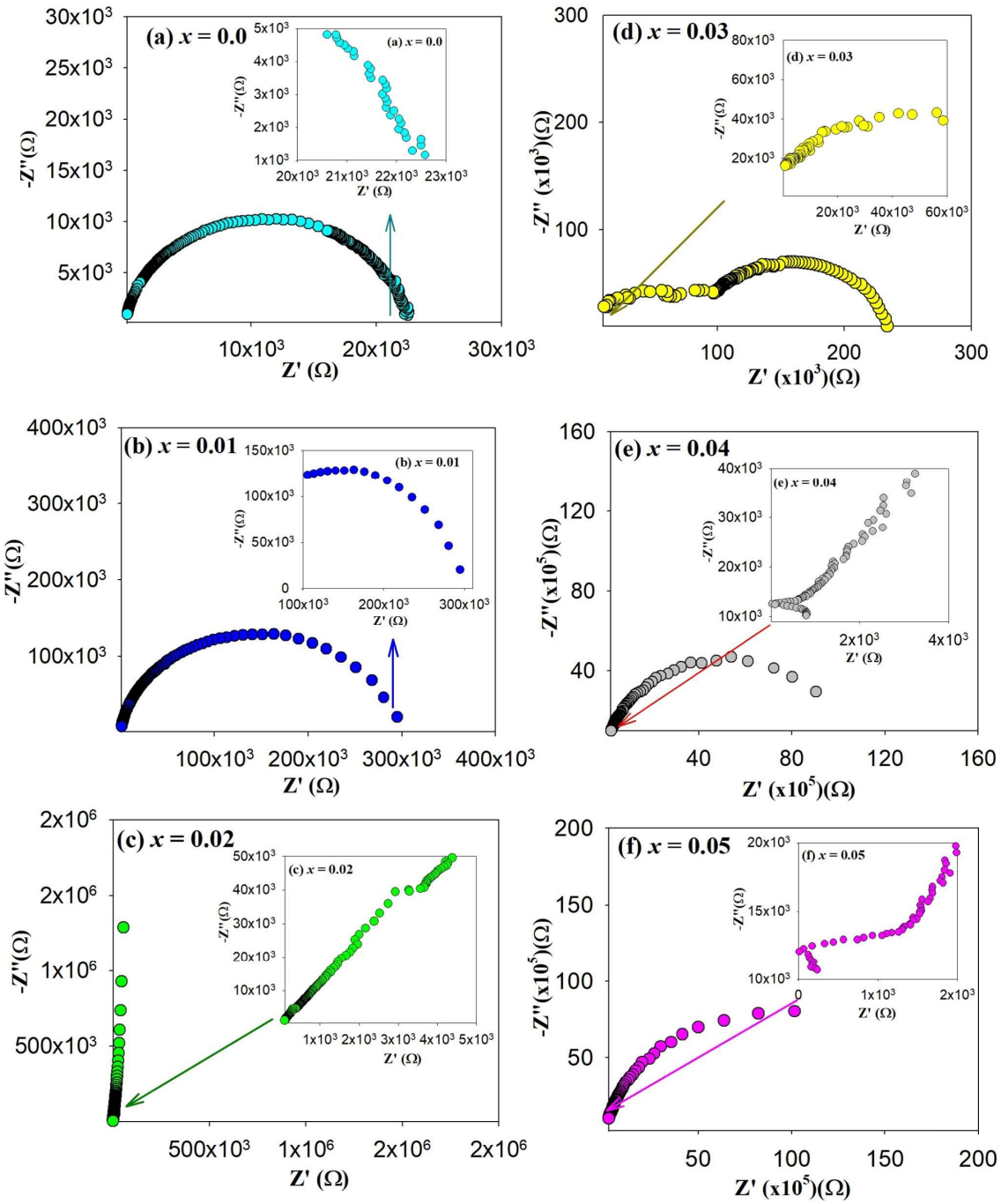

Figure 2. Nyquist plot and electrical equivalent circuit for $Pr_{0.75}Na_{0.05}K_{0.20}Mn_{1-x}Cr_xO_3$: (a) 0, (b) 0.01, (c) 0.02, (d) 0.03, (e) 0.04, and (f) 0.05 compounds at room temperature. Inset: the enlargement of the impedance for all samples at a low frequency region.

3.4. Equivalent circuit

The complex impedance spectra of $Pr_{0.75}Na_{0.05}K_{0.20}Mn_{1-x}Cr_xO_3$ (x = 0–0.05) are modeled using the equivalent circuits shown in the insets of Figure 3, fitted via *Z View 2.0* software. An equivalent circuit model fitting from the Nyquist plot of $-Z''$ as a function of Z' is employed to investigate the electrical behavior and its relationship with the microstructural properties of the compound. The best-fitting composed by the proposed circuit is represented by solid lines in the inset of Figure 3, and

the fitting parameters of R_1, R_2, CPE_1, CPE_2, α_1, and α_2 are listed in Table 1. All samples exhibit semicircular Nyquist arcs, characteristic of resistive-capacitive (RC) relaxation behavior, with the use of constant phase elements (CPEs) in the equivalent circuit models reflecting non-ideal relaxation arising from compositional disorder and microstructural inhomogeneity. The experimental and suggested spectra, as seen, align across the frequency range, indicating that the proposed circuits are acceptable for all samples.

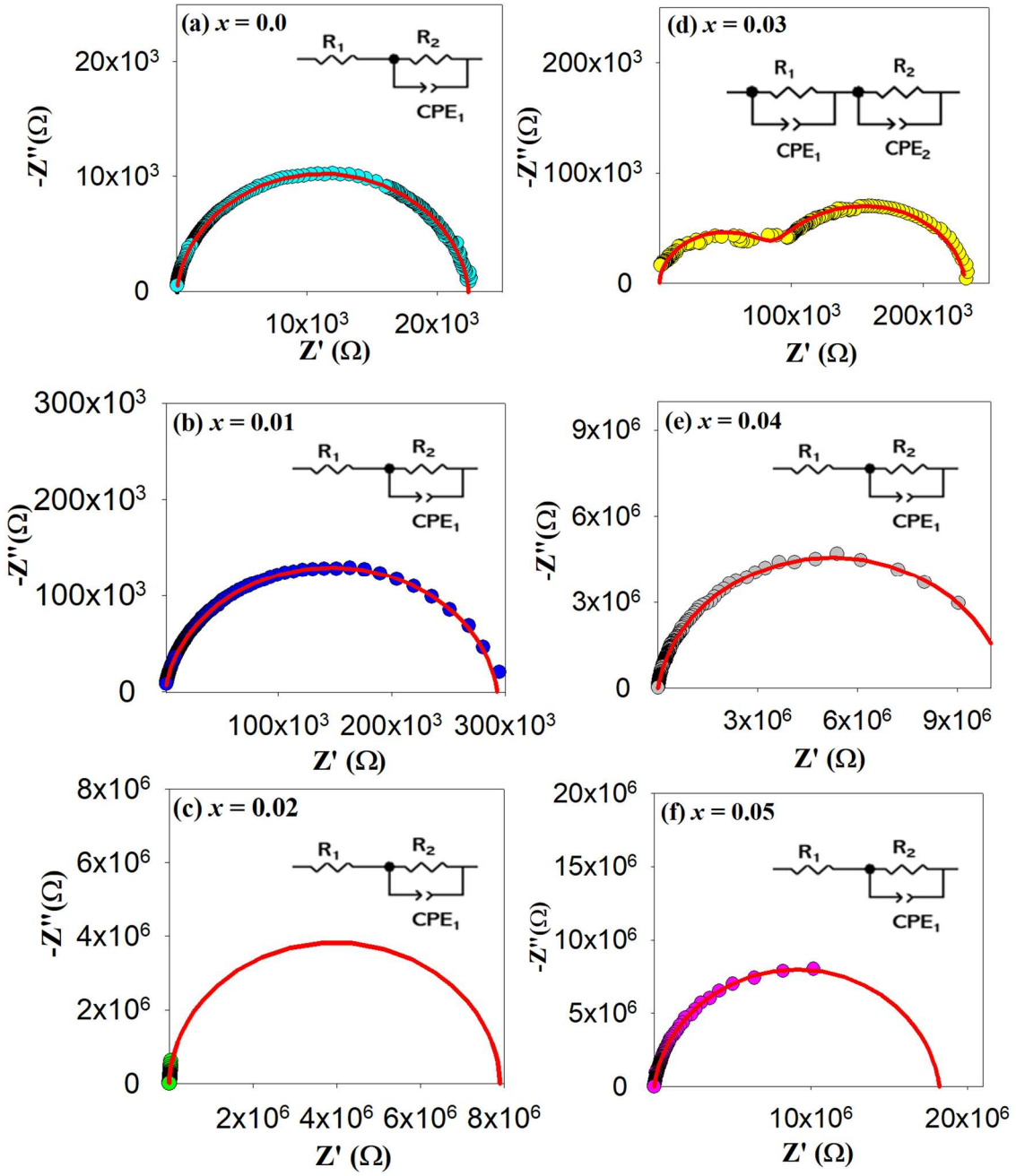

Figure 3. Nyquist plot and electrical equivalent circuit for $Pr_{0.75}Na_{0.05}K_{0.20}Mn_{1-x}Cr_xO_3$: (a) 0, (b) 0.01, (c) 0.02, (d) 0.03, (e) 0.04, and (f) 0.05 compounds at room temperature. The solid red line represents the best fit of possible equivalent circuit in the sample.

As shown in the inset of Figure 3a, the parent compound ($x = 0$) sample has a combination of the RC circuit with the spectra are well-described by the R_1 in series with R_2//CPE_1, where R_1, R_2, and CPE_1 refer to the grain (bulk) resistance, grain boundary resistance, and constant phase element at the grain boundary, respectively. The samples have well-defined single semicircles that indicate efficient bulk conduction with low resistance and near-ideal behavior. Similar circuit model found for $x = 0.01$, with a slight increase in resistance indicates minor disruption in Mn^{3+}/Mn^{4+} interactions. Similar results have been observed in other manganite systems such as in $La_{0.67}Ca_{0.33}Mn_{1-x}Cr_xO_3$ [27]. At $x = 0.02$, the Nyquist plots show a larger semicircle and a high-frequency inclined spike, modeled by R_1 in series with R_2//CPE_1, indicating stronger non-Debye behavior and enhanced localization of charge carriers [28,29]. In addition, it was proposed that the absence of a semicircle arc indicates good ohmic contact between the active material and the current collector [24]. The near-vertical spike suggests improved capacitive behavior, supported by α_{gb}~1 in Table 1 [24].

Further substitution of Cr for $x = 0.03$ exhibits two distinct arcs, indicating a clear separation between grain and grain boundary contributions. The observed behavior can be explained by an equivalent circuit consisting of two parallel equivalent circuits in a series connection [(R_1//CPE_1) + (R_2//CPE_2)], which may relate with two relaxation processes in the samples [30]. (R_1//CPE_1) correspond to contribution of grains at high frequencies, and (R_2//CPE_2) correspond to the contribution of grain boundaries at low frequencies [31]. This dual relaxation process has been reported in related perovskite systems and reflects simultaneous bulk and interfacial polarization mechanisms [32]. Similar results were reported in other manganites systems, such as in $La_{0.7}Bi_{0.3}Fe_{0.5}Mn_{0.5}O_3$ [32].

High substitution of Cr at $x = 0.04$ exhibits a single broad arc, suggesting overlapping relaxation processes or dominant insulating grain boundary effects. This behavior can be described by a similar equivalent circuit (R_1 in series with R_2//CPE_1) as defined above for other compositions. For $x = 0.05$, the very large and distorted arc corresponds to the highest observed resistance, likely caused by Cr-induced defects and deep trapping states [26]. These results imply that the irregular impedance trends stem from a complex interplay between bulk conduction, grain boundary effects, and defect-induced carrier localization than a direct linear dependence on Cr content.

Except for $x = 0.03$, most substituted compositions share a similar equivalent circuit form, though capacitance and α values differ, reflecting changes in relaxation dynamics. Although all compositions share the same equivalent circuit, the values of the circuit elements differ significantly, reflecting changes in the conduction mechanism upon Cr substitution, as summarized in Table 1. The series resistance (R_1) remains relatively small (~10–13 Ω for most samples), and its contribution to the overall response is negligible. Consequently, the associated capacitance is not listed in the table, confirming that the grain boundaries dominate the resistive response of the manganites.

In contrast, R_2 values obtained for all samples are greater than the R_1 (Table 1), confirming that the grain boundaries of insulators play a significant role in the electrical conduction of compounds relative to the grain. This behavior is consistent with the formation of insulating grain boundaries that act as potential barriers to charge transport. Such barriers give rise to Maxwell-Wagner interfacial polarization and the formation of Schottky-type barriers at the grain-grain interfaces [33,34]. A trend is observed with Cr substitution. Both R_2 and the constant phase element (CPE_1) values increase substantially in the Cr-doped samples compared to the undoped composition ($x = 0$). This increase indicates that Cr substitution reduces charge carrier mobility by disrupting the Mn^{3+}–O–Mn^{4+} double-exchange pathway, leading to suppression of the small-polaron hopping mechanism. As a result, the Cr-substituted manganites exhibit poorer conductivity than the unsubstituted sample. The

systematic increase in R_1 and R_2 with Cr content indicates progressive suppression of conductivity due to enhanced electron scattering at disordered grain boundaries [27]. This trend aligns with previous reports for Cr-doped manganite such as in $La_{0.67}Ca_{0.33}Mn_{1-x}Cr_xO_3$ (x = 0–0.20) [27] and $La_{0.7}Ca_{0.3}Mn_{1-x}Cr_xO_3$ (x = 0–0.10), where increased Cr content promotes grain boundary resistance and alters microstructural pathways for conduction [34].

The capacitance values (C) also provide insights into the origin of the dielectric relaxation. For $x = 0$ and 0.01, the capacitance lies in the order of 10^{-10} F, characteristic of grain boundary contributions. With increasing Cr substitution ($x \geq 0.02$), the capacitance decreases to the order of 10^{-11} F, which is typical of bulk or grain contributions. This transition from grain boundary to grain-dominated response indicates that Cr substitution modifies the microstructure and charge distribution within the grains. Notably, at x = 0.03, an additional low-frequency element (CPE_2) appears, with an associated high capacitance (~10^{-5} F) and α_2 close to unity, suggesting strong interfacial polarization due to enhanced space-charge accumulation at grain boundaries or electrode-sample interfaces.

Moreover, the observed increase in R_2 values with increasing Cr content implies a growth in grain size, as reported in in [23]. Larger grains reduce the number of grain boundaries per unit volume, which in turn modifies the balance between grain and grain boundary responses. However, the simultaneous increase in resistive character reflects that Cr acts as an electron localizer, weakening double exchange and increasing charge localization inside the grains.

In summary, the data in Table 1 confirm that electrical conduction in these manganites arises from a complex interplay of grain boundary barriers, bulk grain resistivity, and interfacial polarization. Cr substitution enhances resistive behavior by reducing carrier mobility, shifting the dominant relaxation from grain boundary to grain contributions, and promoting stronger Maxwell-Wagner polarization and Schottky barrier effects at higher doping levels. These findings are consistent with previous studies on Cr-doped manganites [35] and provide strong evidence of the role of microstructural and electronic modifications in governing the impedance response.

Table 1. The equivalent circuit parameters obtained for the $Pr_{0.75}Na_{0.05}K_{0.20}Mn_{1-x}Cr_xO_3$ (x = 0–0.05) manganites deduced from fitting experimental impedance data and the value of capacitance (C) at room temperature (300 K).

Sample, x	R_1 (Ω)	R_2 (Ω)	CPE_1 (F)	α_1	CPE_2 (F)	α_2	C (F)	Response
0.00	10.6	2.24×10^4	7.93×10^{-10}	0.943	-	-	6.03×10^{-10}	GB
0.01	11.0	2.93×10^5	9.92×10^{-10}	0.921	-	-	5.72×10^{-10}	GB
0.02	11.5	7.80×10^6	2.80×10^{-10}	0.990	-	-	2.40×10^{-11}	Grain
0.03	1.46×10^3	8.59×10^6	2.55×10^{-6}	0.970	4.40×10^{-5}	0.95	1.06×10^{-11}	Grain
0.04	13.1	1.05×10^7	5.34×10^{-6}	0.912	-	-	2.76×10^{-11}	Grain
0.05	13.3	1.80×10^7	5.20×10^{-11}	0.916	-	-	3.54×10^{-11}	Grain

The real, Z' and imaginary, Z'' part of the total impedance of the circuit for x = 0, 0.01, 0.02, 0.04 and 0.05 (Figure 3a–c, e,f) are then expressed as Eqs 2 and 3 as follow [14]:

$$Z' = R_1 + \frac{R_2\left(1 + R_2 Q\omega^{\alpha}\cos\left(\frac{\alpha\pi}{2}\right)\right)}{\left(1 + R_2 Q\omega^{\alpha}\cos\left(\frac{\alpha\pi}{2}\right)\right)^2 + \left(R_2 Q\omega^{\alpha}\sin\left(\frac{\alpha\pi}{2}\right)\right)^2} \quad (2)$$

$$Z'' = \frac{{R_2}^2 Q\omega^{\alpha}\sin\left(\frac{\alpha\pi}{2}\right)}{\left(1 + R_2 Q\omega^{\alpha}\cos\left(\frac{\alpha\pi}{2}\right)\right)^2 + \left(R_2 Q\omega^{\alpha}\sin\left(\frac{\alpha\pi}{2}\right)\right)^2} \quad (3)$$

While the expressions for the real, Z' and imaginary, Z'' part of the total impedance for x = 0.03 sample are given as Eqs 4 and 5 [36,37]:

$$Z' = \frac{R_1}{1+\left(\omega R_g Q_g\right)^2} + \frac{R_2}{1+(\omega R_2 Q_2)^2} \quad (4)$$

$$Z'' = \frac{{R_1}^2 Q_1 \omega}{1+(\omega R_1 Q_1)^2} + \frac{{R_2}^2 Q_2 \omega}{1+(\omega R_2 Q_2)^2} \quad (5)$$

where (R_1, Q_1, ω) and (R_2, Q_2, ω) are the resistance, constant phase element, and peak frequency of the grain and grain boundary.

3.5. Dielectric constant

Further investigation is done by plotting the frequency dependence of the dielectric constant (ε') of all samples in $Pr_{0.75}Na_{0.05}K_{0.20}Mn_{1-x}Cr_xO_3$ (x = 0, 0.01, 0.02, 0.03, 0.04, 0.05) at room temperature, as presented in Figure 4. $\varepsilon'(\omega)$ is the real part that describes the storage, and $\varepsilon''(\omega)$ is the imaginary part that describes the loss of energy in the investigated samples during each cycle of the applied electric field (AC). A general decreasing trend of ε' with increasing frequency is observed across all compositions; a behavior commonly associated with the Maxwell-Wagner interfacial polarization and space-charge relaxation at low frequencies. The undoped (x = 0.00) and lightly doped (x = 0.01) samples display high dielectric constants in the low-frequency regime (~10^4), which gradually decrease with frequency. This behavior suggests the presence of strong interfacial polarization and significant grain boundary contributions, in line with semiconducting grain-insulating grain boundary models typically observed in manganite perovskites [24,29].

Interestingly, at x = 0.02, the dielectric response is slightly suppressed compared to the pristine sample, but the overall trend remains similar. A more dramatic change is observed at x = 0.03 and x = 0.04, where ε' decreases substantially across all frequencies, particularly for x = 0.04, which exhibits values as low as ~10^2–10^3. This pronounced suppression of ε' with increasing Cr content can be attributed to the enhanced insulating nature of the grain boundaries induced by Cr substitution. The incorporation of Cr^{3+} at the Mn site likely reduces the density of itinerant electrons (e_g), thereby increasing resistive barriers at grain boundaries and diminishing interfacial polarization [22,24]. Such an effect is indicative of stronger electron localization and reduced polaron hopping, both of which contribute to the dielectric collapse [38].

However, an intriguing anomaly arises at x = 0.05, where the dielectric behavior unexpectedly resembles that of the undoped and x = 0.01 samples than continuing the suppression trend observed at intermediate doping (x = 0.03–0.04). This recovery of ε' could be associated with a compensation

effect, where higher Cr concentration alters the microstructural or electronic properties in a manner that reinstates interfacial polarization. At higher Cr concentrations, several mechanisms may account for the recovery of a dielectric response. First, mixed-valence interactions among Mn^{3+}/Mn^{4+} and Cr^{3+} can stabilize charge carriers, thereby reinstating polarization processes. Second, increased doping may modify the distribution or thickness of insulating grain boundary layers, reduce their blocking effect, and enable dipoles to contribute more effectively [28].

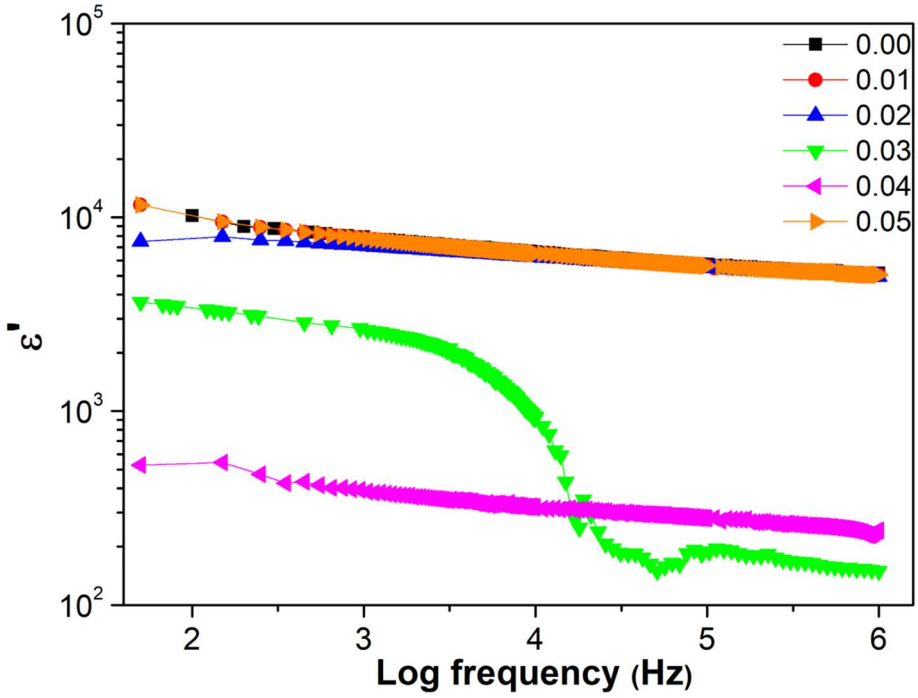

Figure 4. Frequency dependence of dielectric constant (ε') for $Pr_{0.75}Na_{0.05}K_{0.2}Mn_{1-x}Cr_xO_3$ (x = 0–0.05) samples at room temperature.

At higher frequencies, the dipoles are unable to follow the rapidly oscillating electric field, leading to suppression of dielectric response and stabilization of ε' values. As can be seen, all samples exhibit a typical decreasing trend of the ε' with increasing frequency. Such behavior is the characteristics of dielectric relaxation and can be attributed to the Maxwell-Wagner interfacial polarization mechanism, commonly observed in heterogeneous materials such as polycrystalline manganites [39,40]. The findings are consistent with previous reports, which show that microstructural inhomogeneity enhances charge carrier density at grain boundaries, resulting in polarization [38]. At high frequencies, ε' decreases with increasing frequency before reaching a nearly constant value, suggesting that the observed saturation is associated with a relaxation process [39]. In addition, the decrease in ε' with Cr substitution may be due to the structural defect formation properties [41] in the substituted samples [42]. The finding underscores the complex role of Cr substitution in modulating the dielectric behavior of the compounds, with different concentrations leading to distinct dielectric responses [28].

3.6. Dielectric and tangent loss

Figure 5 illustrates the variation of frequency dependence of the dielectric loss or imaginary part (ε'') at room temperature for $Pr_{0.75}Na_{0.05}K_{0.2}Mn_{1-x}Cr_xO_3$ (x = 0–0.05) samples. The unsubstituted (x = 0) ε'' is markedly large in the low-frequency regime, followed by a gradual decay and eventual merging at higher frequencies. This behavior can be rationalized within Maxwell-Wagner and Koop's two-layer models, wherein semiconducting grains are separated by more resistive grain boundary manganite systems [39]. The accumulation of charges at grain boundaries under low-frequency fields produces large interfacial polarization, leading to significant energy loss. Similar low-frequency dielectric relaxation has been consistently reported in manganite systems and related perovskites [22,43]. All Cr-substituted compositions exhibit the characteristic rise of ε'' at low frequencies, followed by a decrease toward the high-frequency limit, confirming that interfacial polarization and charge carrier relaxation dominate the dielectric response. The magnitude of dielectric loss decreases systematically with increasing frequency, reflecting the inability of localized charge carriers to follow the rapidly oscillating field. The x = 0.01 sample stands out, exhibiting extraordinarily high dielectric loss across the full frequency region, surpassing even the parent compound. This enhancement suggests that light Cr substitution promotes increased charge carrier scattering and trapping, thereby elevating energy dissipation. The introduction of Cr^{3+} at the Mn site disrupts the Mn^{3+}/Mn^{4+} double-exchange network, introducing localized states that improve hopping barriers and enhance dielectric relaxation.

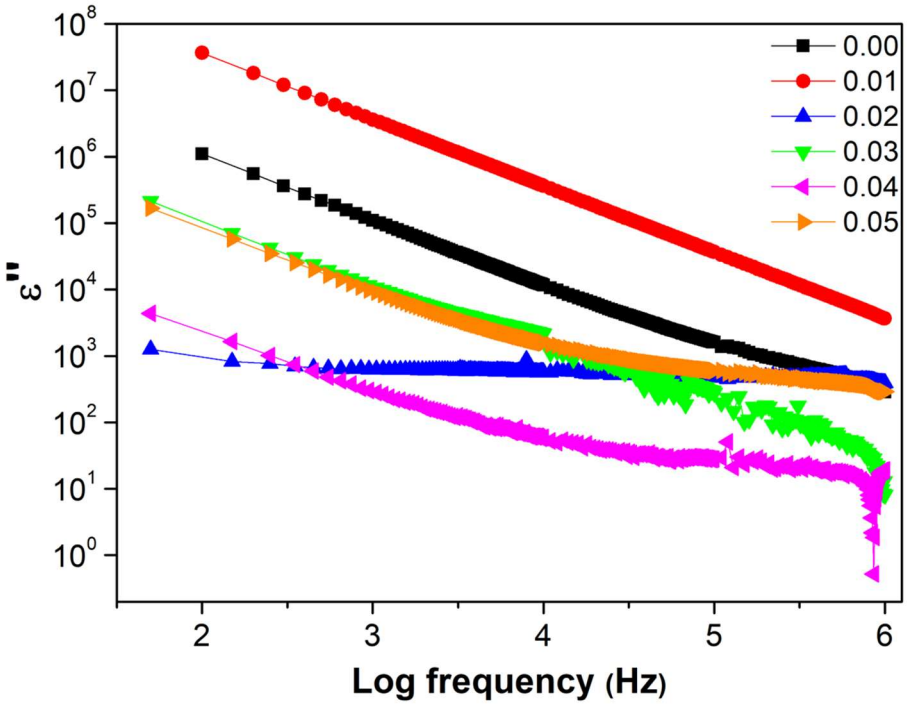

Figure 5. Frequency dependence of dielectric loss (ε'') for $Pr_{0.75}Na_{0.05}K_{0.2}Mn_{1-x}Cr_xO_3$ (x = 0–0.05) samples at room temperature.

As Cr content increases beyond x = 0.01, ε'' decreases markedly, with the x = 0.04 sample showing the lowest loss among all compositions. This suppression of dielectric loss can be attributed to enhanced grain boundary resistivity, which reduces long-range charge motion and limits energy

dissipation. Such suppression is consistent with earlier reports on Cr-doped manganites [44], where higher substitution levels suppress hopping conduction and yield more insulating grain boundaries. Interestingly, at $x = 0.05$, the dielectric loss increases slightly compared to $x = 0.03$–0.04, suggesting a partial recovery of polarization mechanisms. This non-monotonic trend echoes the dielectric constant behavior and may reflect defect-compensation effects, redistribution of grain boundary barriers, or percolation-assisted charge transport at higher doping levels.

From a broader perspective, ε'' represents the energy dissipated by the system under an alternating field. In this series, Cr doping alters both charge-carrier hopping dynamics and grain-boundary characteristics. Light doping ($x \sim 0.01$) enhances loss through defect-mediated scattering and increased carrier localization, whereas heavier substitution ($x \geq 0.03$) suppresses loss by strengthening grain boundary barriers and restricting interfacial polarization. Such compositional tuning of dielectric loss has also been observed in other transition-metal-doped manganites, where defect chemistry and microstructural evolution critically dictate energy dissipation processes [29]. Understanding this dielectric behavior is crucial for tailoring the materials electrical properties for applications such as capacitors [45,46] or sensors [41].

Figure 6 presents the frequency dependence of the loss tangent (tan δ) of $Pr_{0.75}Na_{0.05}K_{0.2}Mn_{1-x}Cr_xO_3$ ($x = 0$–0.05) at room temperature. The tan δ, defined as the ratio of the imaginary (ε'') to the real (ε') components of permittivity, quantifies the extent of energy dissipation within the dielectric medium. Energy loss arises mostly from two processes: Resistive loss, linked to leakage conduction, and relaxation loss, associated with dipolar relaxation dynamics [39].

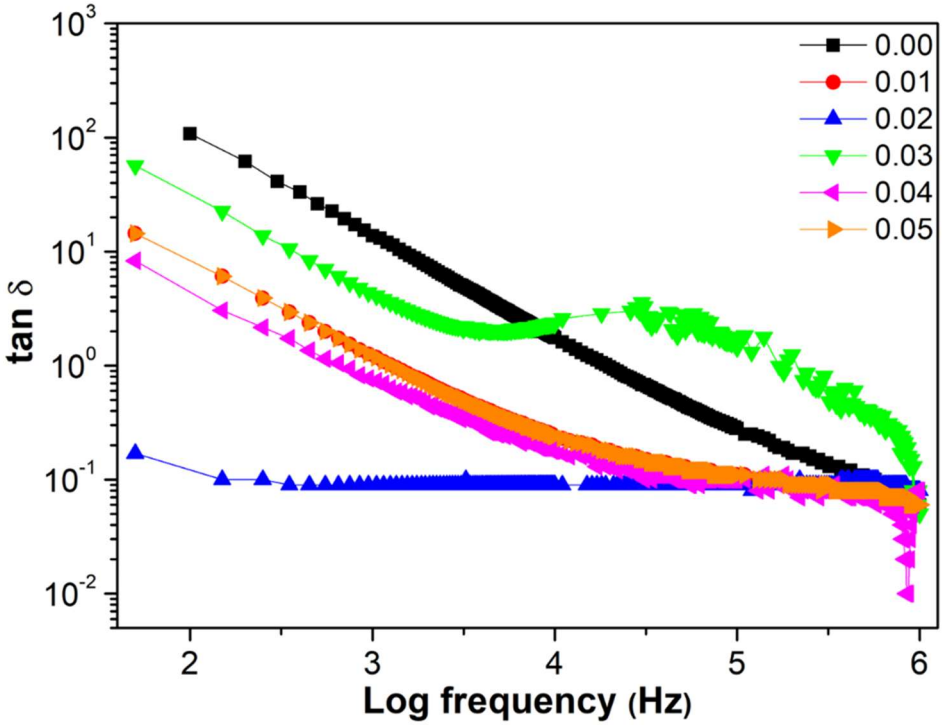

Figure 6. Frequency dependence of tangent loss (tan δ) for $Pr_{0.75}Na_{0.05}K_{0.2}Mn_{1-x}Cr_xO_3$ ($x = 0$–0.05) samples at room temperature.

All samples exhibit relaxation behavior as the tan δ values are high in the low-frequency regime and decrease progressively with increasing frequency before stabilizing in the high-frequency region.

The elevated tan δ at low frequencies reflects substantial charge accumulation at the grain boundaries [47], where the high interfacial resistance requires significant energy for charge migration [25]. This observation is consistent with Maxwell-Wagner type interfacial polarization, frequently reported in manganite perovskites [38]. At higher frequencies, the sharp decline in tan δ suggests that charge carriers require less energy to overcome the reduced resistance of grain boundaries, as the rapid reversal of the alternating field prevents sustained charge accumulation [25,47]. Consequently, dielectric losses become minimal at the high-frequency limit [48].

Compared to the unsubstituted compound, Cr-doped samples show systematically lower loss tangent values, indicating that Cr substitution mitigates the grain boundary resistance effect. This trend suggests that higher Cr levels suppress long-range charge migration and restrict excessive polarization, thereby reducing energy dissipation [14]. Among the compositions, the $x = 0.02$ sample exhibits the lowest tan δ values across almost the entire frequency range, demonstrating exceptional dielectric stability with tan $\delta \approx 0.1$ even at low frequencies. This contrasts with the undoped and lightly doped ($x = 0.01$) samples, where tan δ remains significantly higher (>10) at comparable frequencies.

The consistent decrease in tan δ with frequency across all compositions highlights the improved dielectric performance of Cr-substituted samples at high frequencies. Nonetheless, it is important to note that tan δ exceeds unity in most cases, indicating non-negligible energy loss. Such high values are typical in manganite systems, where mixed-valence conduction and interfacial polarization dominate the dielectric response. The suppression of tan δ upon Cr doping aligns with earlier reports on transition-metal substitution in manganites, where dopants modulate defect chemistry and microstructure to reduce dielectric loss [14,49].

In summary, while all samples display the expected relaxation-type frequency dependence, Cr substitution generally reduces dielectric loss by weakening grain-boundary-related resistive contributions. This improvement, together with the observed stability of the $x = 0.02$ composition, underscores the potential of controlled Cr doping to optimize dielectric performance in Pr-based manganites.

4. Conclusions

Cr substitution in $Pr_{0.75}Na_{0.05}K_{0.20}Mn_{1-x}Cr_xO_3$ ($x = 0.00, 0.01, 0.02, 0.03, 0.04, 0.05$) manganite significantly influences structural and functional properties. Structural analysis confirmed successful Cr^{3+} incorporation into the lattice, with ionic size mismatch driving subtle but systematic variations in unit cell parameters. Microstructural studies revealed that higher Cr content suppresses grain growth, increasing grain boundary density and thereby modifying charge transport pathways. Impedance analysis highlighted a crossover from bulk conduction at low doping to grain boundary-dominated behavior at higher substitution, accompanied by non-Debye relaxation linked to defect states. Dielectric measurements further demonstrated strong frequency-dependent polarization, where moderate Cr doping, particularly at $x = 0.02$, reduced dielectric losses and improved stability. Overall, these findings establish that controlled Cr incorporation is an effective means of tailoring defect chemistry, grain boundary characteristics, and dielectric response in perovskite manganites, providing valuable guidance for designing materials with optimized electrical and dielectric functionalities.

Use of AI tools declaration

The authors declare they have not used Artificial Intelligence (AI) tools in the creation of this article.

Acknowledgments

The authors would like to express their gratitude to the Ministry of Higher Education (MOHE), Malaysia, and Universiti Teknologi MARA for funding this project through the Fundamental Research Grant Scheme (FRGS) (FRGS/1/2019/STG02/UITM/02/2) and Skim Latihan Akademi Bumiputera (SLAB).

Author contributions

Siti Sumaiyah: conceptualization, methodology, investigation, writing–original draft, writing–review & editing; Nor Asmira Amaran: writing–review; Zakiah Mohamed: writing–review; Rozilah Rajmi: writing–review; Sikiru Surajudeen: writing–review; Norazila Ibrahim: supervision, methodology, investigation, validation, formal analysis, writing–review & editing.

Conflict of interest

The authors declare no conflict of interest.

References

1. Guney E, Karimzadeh Khoei J, Sengul BS, et al. (2024) Functional copolymer coatings on electrospun fibers via photo-initiated chemical vapor deposition. *J Appl Polym Sci* 141: e55210. https://doi.org/10.1002/app.55210
2. Zurauskiene N (2023) Engineering of advanced materials for high magnetic field sensing: A review. *Sensors* 23: 2939. https://doi.org/10.3390/s23062939
3. Anwar MS, Ahmed F, Koo BH (2014) Structural distortion effect on the magnetization and magnetocaloric effect in Pr modified $La_{0.65}Sr_{0.35}MnO_3$ manganite. *J Alloys Compd* 617: 893–898. https://doi.org/10.1016/j.jallcom.2014.08.105
4. Gamzatov AG, Batdalov AB, Khanov LN, et al. (2012) Influence of grain boundaries on resistivity of manganites $La_{1-x}K_xMnO_3$. *Phys Solid State* 54: 617–621. https://doi.org/10.1134/S1063783412030110
5. Rozilah R, Ibrahim N, Mohamed Z, et al. (2017) Inducement of ferromagnetic-metallic phase in intermediate-doped charge-ordered $Pr_{0.75}Na_{0.25}MnO_3$ manganite by K^+ substitution. *Physica B Condens Matter* 521: 281–294. https://doi.org/10.1016/j.physb.2017.07.001
6. Hassine A Ben, Dhahri J, Hcini S, et al. (2018) Effects of barium deficiency on structural, magnetic and magnetocaloric properties of $La_{0.6}Nd_{0.1}Ba_{0.3-x}Mn_{0.9}Cr_{0.1}O_3$ manganites. *Phase Transit* 91: 71–82. https://doi.org/10.1080/01411594.2017.1359835
7. Khelifi J, Tozri A, Issaoui F, et al. (2014) The influence of disorder on the appearance of Griffiths phase and magnetoresistive properties in $(La_{1-x}Nd_x)_{2/3}(Ca_{1-y}Sr_y)_{1/3}MnO_3$ oxides. *Ceram Int* 40: 1641–1649. https://doi.org/10.1016/j.ceramint.2013.07.055
8. Denbri F, Mahamdioua N, Meriche F, et al. (2021) A-site Pb doping effect on structural, microstructural and magnetotransport properties of $La_{0.5}Sm_{0.2}Ca_{0.3-x}Pb_xMnO_3$ (x = 0, 0.05, 0.10) manganite. *Mater Chem Phys* 267: 124550. https://doi.org/10.1016/j.matchemphys.2021.124550

9. Saw AK, Channagoudra G, Hunagund S, et al. (2019) Study of transport, magnetic and magnetocaloric properties in Sr^{2+} substituted praseodymium manganite. *Mater Res Express* 7: 016105. https://doi.org/10.1088/2053-1591/ab636d
10. Moualhi Y, M'nassri R, Nofal MM, et al. (2020) Influence of Fe doping on physical properties of charge ordered praseodymium–calcium–manganite material. *Eur Phys J Plus* 135: 809. https://doi.org/10.1140/epjp/s13360-020-00838-2
11. Raveau B, Martin C, Maignan A (1998) What about the role of B elements in the CMR properties of ABO_3 perovskites? *J Alloys Compd* 275–277: 461–467. https://doi.org/10.1016/S0925-8388(98)00372-7
12. Elleuch F, Triki M, Bekri M, et al. (2015) A-site-deficiency-dependent structural, magnetic and magnetoresistance properties in the $Pr_{0.6}Sr_{0.4}MnO_3$ manganites. *J Alloys Compd* 620: 249–255. https://doi.org/10.1016/j.jallcom.2014.09.035
13. Pant P, Agarwal H, Bharadwaj S, et al. (2022) Effects of Cr and Fe substitution at Mn-sites of $GdMn_{1-x}T_xO_3$ (x = 0, 0.10) on its structural and complex dielectric properties. *Mater Chem Phys* 290: 126518. https://doi.org/10.1016/j.matchemphys.2022.126518
14. Abdouli K, Hassini F, Cherif W, et al. (2022) Investigation of the structural, electrical, and dielectric properties of $La_{0.5}Sm_{0.2}Sr_{0.3}Mn_{1-x}Cr_xO_3$ for electrical application. *RSC Adv* 12: 16805–16822. https://doi.org/10.1039/d2ra01006b
15. Zahrin A, Ibrahim N, Mohamed Z (2022) Effects of Bi substitution on electroresistance behaviours in $La_{0.8}BiNa_{0.2}MnO_3$ manganites. *Mater Chem Phys* 292: 126790. https://doi.org/10.1016/j.matchemphys.2022.126790
16. Siwach PK, Singh HK, Srivastava ON (2008) Low field magnetotransport in manganites. *J Phys Condens Matte*r 20: 273201. https://doi.org/10.1088/0953-8984/20/27/273201
17. Raddaoui Z, El Kossi S, Brahem R, et al. (2021) Hopping conduction mechanism and impedance spectroscopy analyses of $La_{0.70}Sr_{0.25}Na_{0.05}Mn_{0.70}Ti_{0.30}O_3$ ceramic. *J Mater Sci Mater Electron* 32: 16113–16125. https://doi.org/10.1007/s10854-021-06160-6
18. Tayari F, Nassar KI, Carvalho JP, et al. (2025) Sol–gel synthesis and comprehensive study of structural, electrical, and magnetic properties of $BiBaO_3$ perovskite. *Gels* 11: 450. https://doi.org/10.3390/gels11060450
19. Kumar N, Kishan H, Rao A, et al. (2010) Structural, electrical, magnetic, and thermal studies of Cr-doped $La_{0.7}Ca_{0.3}Mn_{1-x}Cr_xO_3$ ($0 \leq x \leq 1$) manganites. *J Appl Phys* 107: 08390. https://doi.org/10.1063/1.3342462
20. Gadani K, Keshvani MJ, Dhruv D, et al. (2017) Low field magnetoelectric and magnetotransport properties of sol–gel grown nanostructured $LaMnO_3$ manganites. *J Alloys Compd* 719: 47–57. https://doi.org/10.1016/j.jallcom.2017.05.165
21. Swain A, Anil Kumar PS, Gorige V (2019) Electrical conduction mechanism for the investigation of charge ordering in $Pr_{0.5}Ca_{0.5}MnO_3$ manganite system. *J Magn Magn Mater* 485: 358–368. https://doi.org/10.1016/j.jmmm.2019.04.097
22. Belmabrouk H, Alharbi T (2023) Dielectric properties and conduction mechanism of $La_{0.7}Sr_{0.25}Na_{0.05}Mn_{0.95}Al_{0.05}O_3$ perovskite manganite. *J Taibah Univ Sci* 17: 2204809. https://doi.org/10.1080/16583655.2023.2204809
23. Sumaiyah S, Ibrahim N, Mohamed Z, et al. (2024) Electrical, magnetic, and magnetoresistance studies in chromium-doped Pr-based manganites. *J Mater Sci Mater Electron* 35: 1336. https://doi.org/10.1007/s10854-024-13054-w

24. Manju V, Rohith R, Thejas Prasannakumar A, et al. (2022) Dielectric and electrochemical performance of rhombohedral lanthanum manganite perovskite nanostructures. *New J Chem* 46: 19874–19887. https://doi.org/10.1039/d2nj04213d
25. Achary PGR, Behera S, Choudhary RNP, et al. (2021) Structural, dielectric and electrical properties of cerium-modified strontium manganite ceramics. *J Mater Sci Mater Electron* 32: 5738–5754. https://doi.org/10.1007/s10854-021-05295-w
26. Thakur S, Thakur V, Punia R, et al. (2023) An insight into the temperature-dependent dielectric dispersion and conduction mechanisms in $BaTiO_3$ modified bismuth borate glass-ceramic system. *J Non Cryst Solids* 606: 12–15. https://doi.org/10.1016/j.jnoncrysol.2023.122184
27. Dhahri A, Hcini S, Omri A, et al. (2016) Effect of 20% Cr-doping on structural and electrical properties of $La_{0.67}Ca_{0.33}MnO_3$ perovskite. *J Alloys Compd* 687: 521–528. https://doi.org/10.1016/j.jallcom.2016.06.140
28. Bettaibi A, M'Nassri R, Selmi A, et al. (2015) Effect of chromium concentration on the structural, magnetic and electrical properties of praseodymium-calcium manganite. *J Alloys Compd* 650: 268–276. https://doi.org/10.1016/j.jallcom.2015.05.161
29. Aydi S, Cherif W, Khammassi F, et al. (2021) Microstructural properties, dielectric behaviour, conduction mechanism, impedance, and electrical modulus of $La_{0.65}Ca_{0.25}Sr_{0.1}MnO_3$ manganite. *Appl Phys A* 127: 931. https://doi.org/10.1007/s00339-021-05057-9
30. Moualhi Y, Mleiki A, Rahmouni H, et al. (2022) Investigation of the dielectric response and the transport properties of samarium and strontium-based manganite. *Eur Phys J Plus* 137: 406. https://doi.org/10.1140/epjp/s13360-022-02640-8
31. Rahmouni H, Cherif B, Khirouni K, et al. (2016) Influence of polarization and iron content on the transport properties of praseodymium-barium manganite. *J Phys Chem Solids* 88: 35–40. https://doi.org/10.1016/j.jpcs.2015.09.011
32. Bilkees R, Khan AA, Javed M, et al. (2021) Dielectric relaxation and variable range hopping conduction in sol-gel auto combustion derived $La_{0.7}Bi_{0.3}Fe_{0.5}Mn_{0.5}O_3$ manganite. *Mater Sci Eng B Solid State Mater Adv Technol* 269: 115153. https://doi.org/10.1016/j.mseb.2021.115153
33. Selmi A, Bettaibi A, Rahmouni H, et al. (2015) Physical properties of 20% Cr-doped $Pr_{0.7}Ca_{0.3}MnO_3$ perovskite. *Ceram Int* 41: 11221–11227. https://doi.org/10.1016/j.ceramint.2015.05.072
34. Selmi M, Smida A, Kossi S El (2021) Effect of Polaron formation in conduction and dielectric behavior in $La_{0.7}Sr_{0.25}K_{0.05}MnO_3$ oxide. *J Mater Sci Mater Electron* 32: 6014–6027. https://doi.org/10.1007/s10854-021-05321-x
35. Aakansha, Ravi S (2019) Influence of Cr substitution on magnetic and dielectric properties of gadolinium iron garnets. *Solid State Commun* 300: 113690. https://doi.org/10.1016/j.ssc.2019.113690
36. Ben Jazia Kharrat A, Bourouina M, Moutia N, et al. (2018) Gd doping effect on impedance spectroscopy properties of sol-gel prepared $Pr_{0.5-x}Gd_xSr_{0.5}MnO_3$ ($0 \leq x \leq 0.3$) perovskites. *J Alloys Compd* 741: 723–733. https://doi.org/10.1016/j.jallcom.2018.01.236
37. Chhabra Y, Kumar R, Singh P, et al. (2022) Detailed impedance and electrical studies of Zr^{4+} doped $La_{0.7}Ca_{0.3}(Mn_{0.5}Fe_{0.5})O_3$ for cathode materials in solid oxide fuel cells. *Mater Today Proc* 65: 192–199. https://doi.org/10.1016/j.matpr.2022.06.082

38. Elkossi S, Selmi M, Bourguiba F, et al. (2023) Colossal dielectric response and non-Debye relaxation of $La_{0.7}Sr_{0.25}Na_{0.05}Mn_{0.85}Ti_{0.15}O_3$ ceramic. *Inorg Chem Commun* 153: 110761. https://doi.org/10.1016/j.inoche.2023.110761
39. Bajpai N, Saleem M, Mishra A (2021) Effect of samarium (Sm^{3+}) doping on structural, optical, dielectric and magnetic nature of $La_{1.95}Y_{0.05}NiMnO_6$ double perovskite. *Appl Phys A* 127: 723. https://doi.org/10.1007/s00339-021-04874-2
40. Sharma A, Singh M, Kishore K, et al. (2025) Influence of low sintering temperature on the structural, morphological, and dielectric properties of $(Bi_{0.4}Ba_{0.1})Na_{0.5}TiO_3$ ceramics. *J Mater Sci Mater Electron* 36: 392. https://doi.org/10.1007/s10854-025-14459-x
41. Molak A, Mahato DK, Szeremeta AZ (2018) Synthesis and characterization of electrical features of bismuth manganite and bismuth ferrite: Effects of doping in cationic and anionic sublattice: Materials for applications. *Prog Cryst Growth Ch* 64: 1–22. https://doi.org/10.1016/j.pcrysgrow.2018.02.001
42. Rahangdale KK, Ganguly S (2023) Magneto-dielectric properties of B-site doped (Fe^{3+}, Zr^{4+}) $BiMnO_3$ perovskite ceramic. *Mater Sci Eng B Solid State Mater Adv Technol* 289: 116225. https://doi.org/10.1016/j.mseb.2022.116225
43. Ouni I, Ben Khlifa H, M'nassri R, et al. (2021) Transport properties and dielectric response of $Pr_{0.8}Na_{0.2-x}K_xMnO_3$ (x = 0, 0.05, 0.1, 0.15, and 0.2) ceramics synthesized by sol–gel method. *Appl Phys A* 127: 631. https://doi.org/10.1007/s00339-021-04760-x
44. Ncib W, Ben Jazia Kharrat A, Wederni MA, et al. (2018) Investigation of structural, electrical and dielectric properties of sol-gel prepared $La_{0.67-x}Eu_xBa_{0.33}Mn_{0.85}Fe_{0.15}O_3$ (x = 0.0, 0.1) manganites. *J Alloys Compd* 768: 249–262. https://doi.org/10.1016/j.jallcom.2018.07.192
45. Bourguiba M, Raddaoui Z, Dhahri A, et al. (2020) Investigation of the conduction mechanism, high dielectric constant, and non-Debye-type relaxor in $La_{0.67}Ba_{0.25}Ca_{0.08}MnO_3$ manganite. *J Mater Sci Mater Electron* 31: 11810–11818. https://doi.org/10.1007/s10854-020-03733-9
46. Phillips J (2018) Toward an improved understanding of the role of dielectrics in capacitors. *Materials* 11: 1–15. https://doi.org/10.3390/ma11091519
47. Baazaoui M, Moulahi A, Hamdaoui N, et al. (2021) Study of the dielectric behavior as a function of the frequency at different temperatures on the sample $Pr_{0.525}Y_{0.075}Ca_{0.1}Sr_{0.3}Mn_{0.975}Fe_{0.025}O_3$. *Int J At Nucl Phys* 6: 025. https://doi.org/10.35840/2631-5017/2525
48. Bharathi M, Anuradha KN, Murugendrappa MV (2023) Structural, AC conductivity, dielectric and impedance studies of polypyrrole/praseodymium calcium manganite nanocomposites. *Dig J Nanomater Biostruct* 18: 343–365. https://doi.org/10.15251/djnb.2023.181.343
49. Ben Jazia Kharrat A, Moutia N, Khirouni K, et al. (2018) Investigation of electrical behavior and dielectric properties in polycristalline $Pr_{0.8}Sr_{0.2}MnO_3$ manganite perovskite. *Mater Res Bull* 105: 75–83. https://doi.org/10.1016/j.materresbull.2018.04.035

AIMS Press